Metal-support interaction promoted multifunctional electrocatalysis on PtCo/NC with ultralow Pt loading for oxygen reduction reaction and zinc-air battery

Manting Zhang, Tingting Zhou, Danil Bukhvalov, Fengyan Han, Caiqin Wang [*], Xiaofei Yang [*]

College of Science, Nanjing Forestry University, Nanjing 210037, Jiangsu, China

A B S T R A C T

Tri-functional PtCo/NC nanocatalysts were assembled via in-situ integration with ultralow Pt loading supported on ZIF-67 derived porous carbon material, and used as electrocatalysts for oxygen reduction reaction (ORR), ethanol oxidation reaction (EOR), hydrogen evolution reaction (HER). Detailedly, PtCo-3/NC with ultralow Pt loading (1 wt%) exhibits the halfwave potential of 0.877 V for ORR in acidic media and considerable current density for both ORR and EOR at 0.85 V, and low overpotential (η_{10} =10 mV) for HER. The as-assembled zinc-air batteries (ZABs) based on PtCo/NC have higher power density than Pt/C based ZABs. DFT calculation reveals the strong metal-support interactions (MSI) in PtCo/NC, which leads to the change of electronic state, redistribution of charge density and optimization of free energy, allowing it to present greater performances than Pt/C. This work highlights the possibility of using it as highly effective electrode catalysts with ultralow Pt loading in fuel cells and metal-air battery.

1. Introduction

Fuel cells and zinc-air batteries (ZABs), which convert chemicals into electrochemical energy through oxygen reduction and fuel molecules (such as ethanol and H_2, etc.) oxidation reactions, are important energy conversion devices with great promise in the future energy system due to their high energy density and environmental friendliness [1–4]. The reactions involved in those energy conversion process are generally kinetically sluggish and have large reaction energy barrier, resulting in unsatisfying power density and poor durability of the devices [5–7]. Therefore, efficient electrocatalysts are required for these reactions to ensure fast electron and mass transfer, lower the reaction energy barrier, and provide abundant tri-phase regions for surface reaction, ultimately improving the energy efficiency [8,9]. Pt has been widely regarded as the state-of-the-art electrocatalyst for these reactions. However, the high cost and poor durability seriously impede the use of pure Pt catalysts in the large-scale commercial applications [1,4,10–12]. Hence, developing low-cost, highly efficient, and durable electrocatalysts is of utmost importance to solve the above mentioned issues [1,13–16].

Fabricating Pt-M (M represents transition metals) alloy/bimetal materials is considered to be a promising way in addressing the application in the energy conversion devices [16]. Remarkably, PtCo nanoparticles have been widely used in Toyota Mirai fuel cell vehicles since 2015, further hinting the commercialization potential of PtCo catalysts [17]. Recent studies have revealed that a sort of transition metal nanoparticles derived from metal-organic frameworks (MOF) have the unique advantages in fabricating efficient Pt-based alloy/bi-metal materials [18], such as PtCo/NC [19,20], PtZn/NC [21,22]. Via the carbonization and/or hydrogenation, transition metal species are reduced and supported on N-doped porous carbon materials (denoted as M-N-C), which makes the metal species strongly adhere on N-doped porous carbon materials, and thus the aggregation of metal species be inhibited during carbonization due to the rigid crystal structure, achieving to highly exposed active sites and superior electrical conductivity, facilitated mass transfer and ultimately improved utilization efficiency [21,23,24]. In addition, the polyhedral morphology of the MOF-derived catalysts is always favorable to improve the surface area and mass transportability, which play a vital role in the activity of the catalysts [25,26].

Moreover, the residual heteroatoms (such as nitrogen and corresponding transition-metal elements (Fe, Co, Mn, Cu, Zn, etc.) in M-N-C could form the incorporation of heteroatoms to change the charge environment and develop well defined heteroatom functional groups as well as intrinsic redox active sites [27,28]. For example, it has been

proved that owing to the existence of high density pyridinic-N sites in Zn-N-C, the carbon atoms neighboring the pyridine nitrogen become the basis of ORR active site for the further development of highly active catalysts [29]. DFT calculations also unveiled that the 3*d* orbital electrons in Co would enhance the interplay of electrons in the *d* orbitals between Co and Pt, which allows the redistribution of charge, lowers *d*-band center on Pt and finally enhances the catalytic activity [30–32]. These aspects would lead to strong metal-support interactions (MSI) between Pt and M-N-C, thus resulting in the improvement of overall catalytic activity [33–35]. However, there are few reports expounding what MSI are like in Pt-M/NC and what is the mechanism that the electrocatalytic activity promoted by MSI.

Based on these considerations, we designed PtCo/NC bimetallic catalysts with ultra-low platinum loading through a partial galvanic replacement reaction between Pt ions and ZIF-67 derived Co/NC in this work. The as-assembled nanomaterials have several advantages for electrocatalysis: Firstly, in-situ integration contributes to strong adhesion between Pt nanoparticles and the Co/NC substrate. Secondly, the porous carbonaceous structure not only facilitates the mass as well as electrons transfer in catalysis, but also allows homogeneous Pt nanoparticles to expose more active sites. More importantly, theoretical calculation results based on DFT in this work claimed that the metal-support interactions (MSI) between Pt and Co/NC substrate, including the effect of electronic structure, the charge density redistribution, and optimized free energy, would lead PtCo/NC to be more energetically favorable than Pt/C. As a result, PtCo/NC samples show excellent catalytic performances toward oxygen reduction reaction (ORR), ethanol oxidation reaction (EOR), hydrogen evolution reaction (HER). Most strikingly, the PtCo-3/NC with ultralow Pt loading (1 wt%) exhibits outstanding catalytic performances in acidic media in terms of mass activity. The as-assembled zinc-air battery (ZAB) based on PtCo/NC catalysts as anode electrode also have comparable specific power density to commercial Pt/C based zinc-air battery.

2. Experimental

2.1. Materials

Co(NO$_3$)$_2$·6 H$_2$O and K$_2$PtCl$_4$ are purchased from Shanghai Aladdin Bio-Chem Technology Co., Ltd. 2-methylimidazole are purchased from Sigma-Aldrich (Shanghai) Trading Co., Ltd. Absolute methanol is purchased from American TEDIA Co., Ltd. Absolute ethanol, isopropanol, HClO$_4$, H$_2$SO$_4$ and KOH are purchased from Sinopharm Chemical Reagent Co. Ltd. 5 wt% Dupont Nafion membrane solution was obtained from Suzhou Sinero Technology Co., Ltd. All chemicals are used as received without any further purification.

2.2. Synthesis of PtCo-X/NC derived from ZIF-67

Firstly, ZIF-67 was prepared by a typical liquid phase coordination method [36]. In detail, 0.29 g of Co(NO$_3$)$_2$·6 H$_2$O was dissolved in 25 mL of absolute methanol, and the solution was getting light-red, denoted as solution A. In another container, 0.32 g of 2-methylimidazole was dissolved into 25 mL of absolute methanol, too, which was labeled as solution B. The resulting solution B was then quickly added into the solution A with strong stirring for 10 min. The mixture solution was laid down for 24 h at room temperature. After that, the products of purple precipitate were washed with absolute methanol for five times, then collected and dried at 60 °C in vacuum for 6 h. The final powders are assigned as ZIF-67.

To obtain PtCo/NC bimetallic catalysts derived from ZIF-67, the ZIF-67 precursors were primarily calcined in an atmosphere with 5 % H$_2$ in Ar to 435 °C (2 °C min^{-1}) for 8 h and then naturally cooled to obtain cobalt nanoparticles confined in N-doped carbon matrix (Co/NC). Then, 21 mg of Co/NC was dispersed 3 mL of K$_2$PtCl$_4$ solution (31.3473 mg/ mL) to proceed partial galvanic replacement reaction between metallic

Co and Pt ions (Scheme 1). The time of replacement reaction was controlled to be 3, 6, 9 and 12 h, respectively, which would result in different loading of Pt on it. Finally, the products were washed with ultrapure water and dried by freeze-drying. The resulting catalysts supported on N-doped carbon matrix was assigned as PtCo-X/NC (X = 3, 6, 9 and 12), in which the loading amount of Pt on each electrode is characterized to be 1.25 mg/L, 7.94 mg/L, 13.41 mg/L, 19.07 mg/L by ICP, corresponding to 1 %, 10 %, 17 %, and 25 %, respectively. The mass percentages of Co and atomic ratio of Pt and Co elements in a series of PtCo/NC samples were also summarized in Table S1.

2.3. Characterizations

In order to obtain the information about morphology and element distribution of the samples, a scanning electron microscopy (SEM, JSM-7600 F, Japan) is used. Energy-dispersive X-ray Spectroscopy (EDS) and transmission electron microscopy (TEM) are carried out by a JEM-1400 equipment, which runs at 200 keV in order to obtain the microstructure and element distribution of the samples. X-ray diffraction (XRD) is conducted by a Rigaku Ultima IV instrument using Cu Kα radiation (λ = 1.54178 Å) as X-ray source with the scan range of 10°-80° to analyze the sample structure. Inductively coupled plasma-mass spectrometry (ICP-MS) is conducted using PE Optima 800 instrument. X-ray photoelectron spectroscopy (XPS) is conducted by a RBD upgraded PHI-5000CESCA system (Perkon-Elmer) using Al Kα radiation (*hν* = 1486.6 eV).

2.4. Electrochemical measurements

Electrochemical measurements were performed via a typical three-electrode system on a CHI 760E electrochemical analyzer (CH Instruments, Inc., Shanghai), in which a glassy carbon electrode (GCE) or rotating disk electrode (RDE) (Pine Instruments, Grove city, PA) with catalyst was used as working electrode, graphite rod electrode as counter electrode, and reversible hydrogen electrode (RHE) as reference electrode. The HClO$_4$ solution, H$_2$SO$_4$ solution and KOH solution with/ without ethanol were used as electrolyte for electrochemical measurements, respectively. Linear sweep voltammetry (LSV) polarization curves are recorded at a scan rate of 5 mV s^{-1}, cycles voltammetry (CV) was carried out with a scan rate of 50 mV s^{-1}. All data were presented without IR compensation. The current density recorded in ORR, EOR, and HER was normalized with the geometric area (geo) of work electrodes.

A well-dispersed catalyst ink was prepared as below: 1.0 mg of sample and 0.5 mg of carbon black were dispersed into 100 μL of a mixture containing isopropanol and 5 wt% Nafion, then sonicated for 30 min. Subsequently, the ink containing 0.1 mg of catalyst was dropped onto the surface of work electrode and dried at room temperature for use.

2.5. Calculation method

The atomic structure and energetics of various configurations was studied by DFT using the QUANTUM-ESPRESSO code [37] and the GGA-PBE [38], taking into account van der Waals forces correction [39]. For all calculations we used ultrasoft pseudopotentials [40]. The values of energy cutoffs of 25 Ry and 400 Ry were used for the plane-wave expansion of the wave functions and the charge density, respectively. The enthalpy of reaction was defined as difference in calculated total energies of products and reactant. The method of the calculation of the Gibbs free energies were adopted from previous theoretical works [41–44]. For the modeling of ORR, overpotential of U = 1.23 eV was used [43,44].
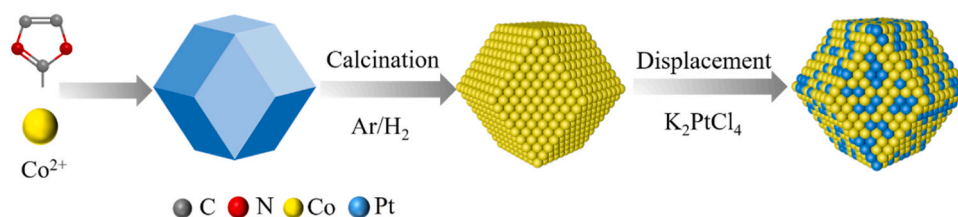
Scheme 1. Schematic diagram of the synthesis for PtCo-X/NC.

3. Results and discussion

The morphology of PtCo/NC bimetallic materials, ZIF-67 precursors and Co/NC are shown in Fig. 1 and Figs. S1–3, respectively. It can be seen from Fig. S1 that the as-synthesized pure ZIF-67 particles present a typical regular dodecahedron with smooth surface and uniform size. Co/
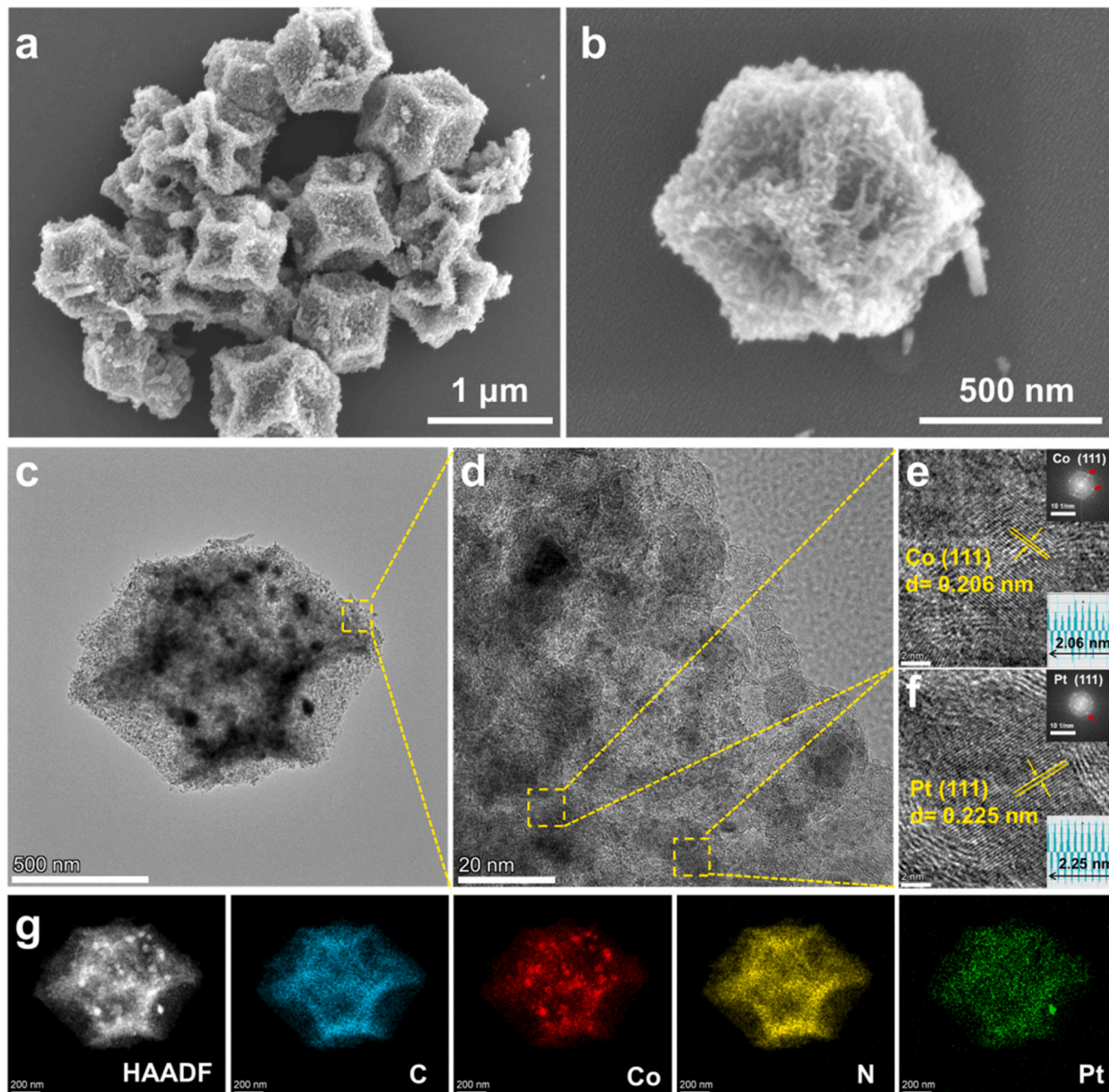

Fig. 1. (a, b) SEM images of PtCo-3/NC nanoparticles; (c) TEM and (d) HR-TEM images of PtCo-3/NC; (e, f) HR-TEM images Co and Pt nanoparticles in PtCo-3/NC, and the insets on the top right are the diffraction pattern calculated using an FFT of the HR-TEM images, respectively; (g) HAADF-STEM of PtCo-3/NC nanoparticle and its corresponding element mapping images.

NC obtained via calcination maintains the polyhedral framework (Fig. S2), while the surface is getting rough and slightly shrunk with dent. After the replacement reaction with the Pt, for instance, PtCo-3/NC nanoparticles (Fig. 1a and b), it can be seen that there are many fiber-like nanoparticles growing on the surface. As the replacement time extends, such as PtCo-6/NC, PtCo-9/NC, and PtCo-12/NC shown in Figs. S3, the fiber-like nanoparticles are growing into nanorods attached on the surface (Figs. S3b, e, and h), while the size and shape do not change a lot. And the EDS spectra in Figs. S3c,f, and i confirm that Co and Pt elements exist in PtCo/NC samples, and the insets on top right are the atomic fraction of Pt and Co according to the EDS spectra. The microstructure of PtCo-3/NC is further examined via TEM and HR-TEM (Fig. 1c-f). As seen, Pt nanoparticles are distributed and anchored on the carbon carrier; the in-situ integration contributes to strong adhesion between the hybrid Pt catalyst and N-doped C support. Fig. 1e and f are the HR-TEM images, from which the crystal lattice can be observed clearly; in detail, the lattice space of 0.206 nm is corresponding to Co (111) plane, and the lattice space of 0.225 nm is attributed to Pt(111) plane of face-center cubic Pt. Fig. 1 g shows the HAADF-STEM image of PtCo-3/NC and the corresponding EDS mapping images. It can be seen that after the displacement reaction between Co and Pt ions, Pt is deposited and mainly distributed in the same area as Co; meanwhile, C and N are uniformly distributed on the Co/NC surface, indicating the nitrogen doped in the carbon matrix. The similar information can be obtained on PtCo-6/NC and PtCo-9/NC from Figs. S4 and S5; the lattice observed in the HR-TEM as well as the electron diffraction patterns further confirmed the coexistence of Co and Pt in the PtCo/NC samples. From the above SEM and TEM images, it is supposed that Co is partially displaced by Pt successfully, and the polyhedral framework of PtCo/NC catalysts is still well maintained although the displacement time increases. Meanwhile, the remaining nitrogen in carbon matrix could form the nitrogenous microenvironment in the catalysts, which is expected to be beneficial for the improvement of the catalytic and stability of catalyst materials [19,20,45].

The XRD patterns shown in Fig. S6 are used to further study the crystal structure of the as-prepared PtCo/NC catalysts. When the replacement time is 3 h, there is no obvious characteristic diffraction peak of Pt, while the replacement time increases to 6 h, the diffraction peak of Pt(111) is observed at around 39.5°. As the replacement reaction goes on, the intensity of the diffraction peak of Pt increases, but the peak intensity of Co gradually decreases, which is consistent with the results of ICP summarized in Table 1. It is probably due to the fact that with the increase of the replacement time, the loading of Pt increased on the catalyst surface, and Co was gradually resolved during the replacement reaction with Pt [46]. XPS test was executed to further investigate about the change in oxidation states and dual metal interactions during Pt addition on Co/NC and PtCo-3/NC. Fig. 2a is XPS spectra of survey scan for Co/NC and PtCo-3/NC, respectively, and Fig. 2b shows the high-resolution XPS spectra of Pt 4 f in PtCo-3/NC. The spectra could be resolved to three well-separated doublets, in detail, the peaks at 71.4 eV and 74.8 eV are assigned to Pt^0 4 $f_{7/2}$ and Pt^0 4 $f_{5/2}$ of the metallic Pt generated after the displacement reaction; while the main peaks at 72.8 eV and 76.1 eV are attributed to Pt 4 $f_{7/2}$ and Pt 4 $f_{5/2}$ of Pt^{2+}, and

peaks at 74.4 and 77.8 eV attributed to Pt 4 $f_{7/2}$ and Pt 4 $f_{5/2}$ of Pt^{4+}, which are corresponding to PtO and PtO_2, respectively [47,48]. The high-resolution XPS spectra of C 1 s in both Co/NC and PtCo-3/NC shown in Fig. 2c can be deconvoluted into three peaks, including C-C/C=C (284.8 eV), C-N (285.5 eV) and C-O (289.1 eV) [49]. The presence of the C-N peak verifies that nitrogen was doped in the carbon skeleton [50]. The N 1 s peaks in Fig. 2d can be fitted into three different components: pyrrolic-N, graphitic-N and pyridinic-N, respectively, indicating that N element from 2-methylimidazole is doped into the porous carbon matrix [49,51]. According to previous reports, the addition of nitrogen to the carbon carrier could possibly enhance its electron-donor ability and enable fast ion diffusion during electrochemical evaluation, thus boosting the catalytic process [50,52,53]. It is worth to note that, compared to the N 1 s peaks in Co/NC, these three deconvoluted N 1 s peaks of PtCo-3/NC slightly shift to lower binding energy after Pt metal being introduced, indicating that the surface active site of PtCo-3/NC has a high electron cloud density, which is owing to the effective electron transfer between metal-support interactions (MSI) [34,35]. Fig. 2e shows the XPS spectra of Co 2p in Co/NC and PtCo-3/NC, respectively. The Co 2p spectra of Co/NC can be deconvoluted into six peaks: the peaks at 779.1 and 794.1 eV, as well as the peaks at 781.1 and 796.1 eV can be attributed to 2p peaks of Co^0 and Co^{2+}, respectively; and the peaks at 785.5 and 802.9 eV are a pair of satellites (sat.) peaks [54]. However, after incorporation with Pt metal, all peaks of Co 2p in PtCo-3/NC shift to higher state compared to that in Co/NC. In detail, the center of peaks of Co^0 2p shifts to 780.0 and 795.1 eV, the peaks of Co^{2+} 2p shift to 781.9 and 796.8 eV, respectively, as shown in Fig. 2e. This results indicate that the electronic structure of Co was regulated effectively after introducing Pt [55]. The signals of Co and Pt verify the coexistence of Pt and Co in the PtCo-3/NC sample after partial replacement, while the shift of peaks in binding energy indicates the modulation of electronic structure in the catalysts. XPS spectra of PtCo-6/NC is shown in Fig. S7, from which it can be seen that there is no obvious difference in the shift of the peaks compared with that of PtCo-3/NC.

To evaluate the electrocatalytic activity of PtCo/NC catalysts, the as-prepared samples were mixed with the commercial carbon black (XC-72) to prepare the carbon-loaded catalysts. CV curves are first measured in 0.5 M H_2SO_4 (Fig. S8a). The peaks clearly observed in the range of 0–0.3 V on all electrodes are attributed to the characteristic hydrogen adsorption and desorption on Pt, which can be used to evaluate the electrochemical active surface area (ECSA). The ECSA values are 224.37, 44.05, 27.02, 20.04 m^2 g_{Pt}^{-1} for PtCo-3/NC, PtCo-6/NC, PtCo-9/NC and PtCo-12/NC, respectively (summarized in Fig. S8b), while it is 32.53 m^2 g_{Pt}^{-1} on Pt/C. The electrocatalytic ORR performances of the as-prepared PtCo/NC catalysts and Pt/C are evaluated using a rotating disk electrode (RDE) in O_2-saturated $HClO_4$ (0.1 M). Fig. 3a shows the linear sweep voltammetry (LSV) curves of the PtCo-3/NC, PtCo-6/NC, PtCo-9/NC and PtCo-12/NC, respectively. The PtCo-9/NC with 17 % of Pt loading exhibit $E_{1/2}$ of 0.898 V, which is very close to Pt/C (0.901 V), while PtCo-12/NC catalysts with a little higher Pt loading exhibit higher $E_{1/2}$ (0.920 V) than Pt/C. By contrast, PtCo-6/NC with much lower Pt loading presents $E_{1/2}$ of 0.886 V, which is comparable to Pt/C; especially

Table 1
The summarized Pt loads (wt%), catalytic activities for ORR and EOR in acidic and alkaline media on all PtCo/NC and Pt/C catalysts, respectively.

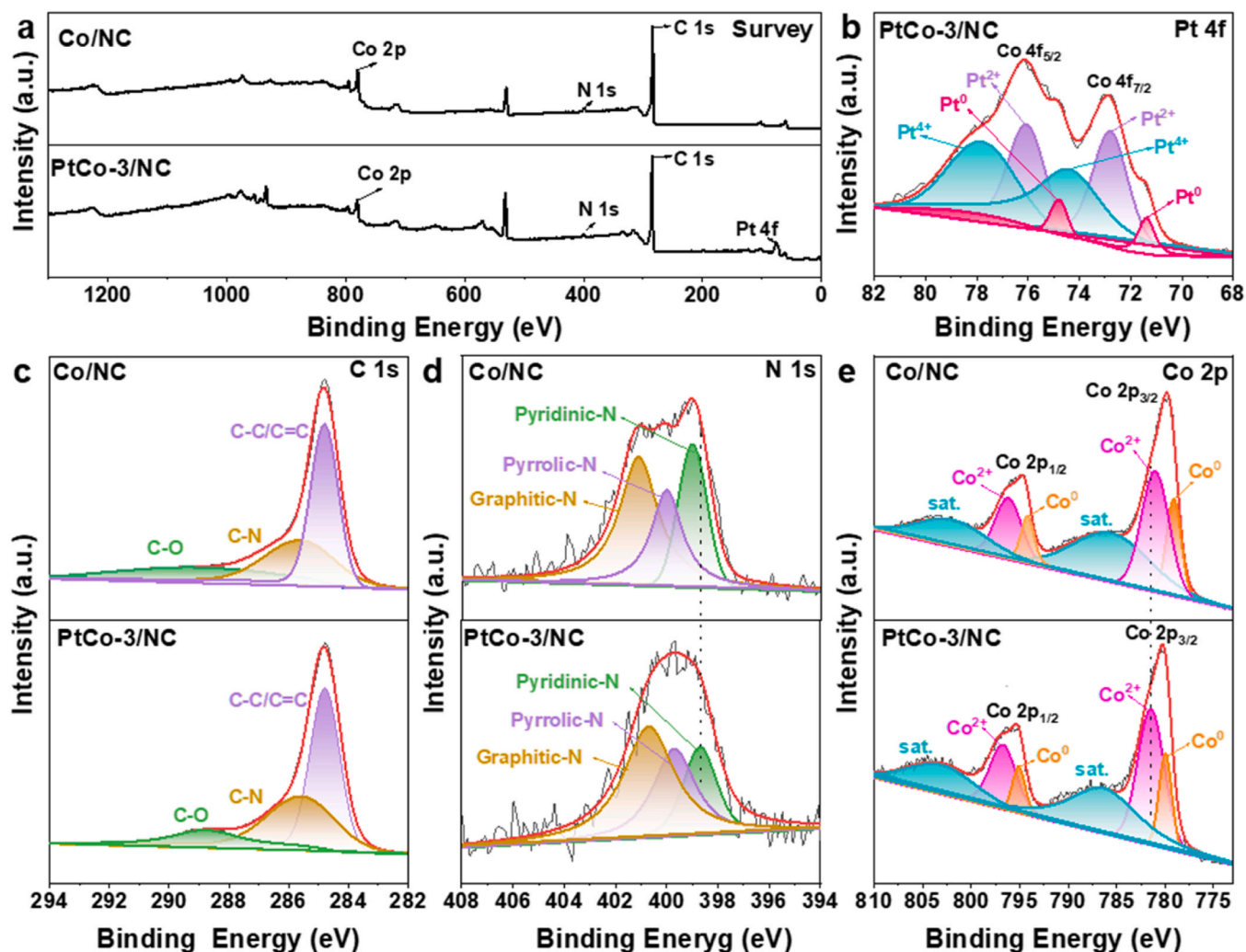| Electrodes	Pt / %	ORR				EOR	
		0.1 M $HClO_4$		0.1 M KOH		$C_2H_5OH/HClO_4$	$C_2H_5OH/$ KOH
		$E_{1/2}$/V	j_k at 0.85 V	$E_{1/2}$/V	j_k at 0.85 V	$j_{at\ 0.85\ V}$	$j_{at\ 0.85\ V}$
PtCo-3/NC	1 %	0.877	11.18	0.859	6.72	14.47	24.56
PtCo-6/NC	10 %	0.886	15.11	0.864	7.61	19.01	27.26
PtCo-9/NC	17 %	0.898	19.98	0.884	11.97	22.43	33.84
PtCo-12/NC	25 %	0.920	34.20	0.886	12.36	23.78	45.32
Pt/C	20 %	0.901	21.94	0.895	20.08	17.62	50.4

Fig. 2. (a) XPS spectra of survey for Co/NC and PtCo-3/NC; (b) XPS spectra of Pt 4 f of PtCo-3/NC; XPS spectra of (c) C 1 s, (d) N 1 s and (e) Co 2p of the Co/NC and PtCo-3/NC, respectively.

PtCo-3/NC with ultralow Pt loading of 1 %, it also exhibits comparable $E_{1/2}$ (0.877 V) to many similar materials with high Pt loading as summarized in Table S2. Tafel slope can be calculated via the Koutecky-Levich equation according to ORR polarization curves [56,57], recorded in Fig. 3b. Note that although PtCo-3/NC has ultralow Pt loading, the Tafel slope on it is close to Pt/C, indicating the rapid ORR kinetics on PtCo/NC catalysts. Meanwhile, the kinetic current density (j_k at 0.85 V) are summarized as histograms in Fig. 3c. PtCo-12/NC also presents the highest kinetic current density (j_k at 0.85 V) of 34.2 mA cm_{geo}^{-2}, which is about 1.6 times as high as that on Pt/C in 0.1 M $HClO_4$. It can be noted that PtCo-9/NC with lower Pt loading presents similar kinetic current density to Pt/C, and PtCo-3/NC with ultralow Pt loading shows comparable (even higher) performance than some similar Pt-based catalysts with more Pt loading in the literature (summarized in Table S2), evidencing that the Co/NC substrate in PtCo/NC catalysts primarily contributed to enhance ORR activity. The ECSA-normalized j_k are also summarized in Fig. S9.

To further investigate the ORR activity on PtCo/NC catalysts, the electron transfer number were determined using a rotating disk electrode (RDE). From the polarization curves obtained at different rotation rates, the average electron transfer number (n) for PtCo/NC catalysts is calculated as ca. 3.6 in the potential range of 0.3–0.7 V (as depicted in Fig. S10), corroborating a 4e⁻ oxygen reduction pathway [58–60]. This is close to that of the benchmark Pt/C (3.6, Fig. S11) in this work. Based on the above results, the long-term stability of the PtCo/NC catalyst were

further examined via the CVs for 15,000 cycles in the potential range of 0–1 V (vs. RHE). The CVs were recorded every 5000 cycles and LSV curves were also subsequently inspected for comparison. As shown in Fig. S12, there are tiny difference in the half-wave potential of the ORR after 15,000 cycles on those PtCo/NC-based electrodes, which is also comparable to that on Pt/C (Fig. S13), illustrating the superior electrochemical stability of the as-prepared PtCo/NC catalyst. The post morphology of PtCo-3/NC was studied to investigate the dispersion of atomic Pt and Co in carbonaceous matrix after prolonged durability via 5000 cycles of CVs in 0.1 M $HClO_4$ solution, shown in Fig. S14. As seen, PtCo-3/NC nanoparticles after prolonged durability still keep the polyhedral structure and the size, while the fiber-like nanostructure of nanoparticles on the surface of PtCo-3/NC are disappearing after 5000 cycles of continuous cyclic voltammetry tests, resulting that the surface is getting blunted. Additionally, from the element mapping, it can be seen that Pt and Co are still dispersed evenly in carbonaceous matrix of PtCo-3/NC after prolonged durability. Note that the atomic fraction of Co shown in the inset tables decrease a lot after prolonged durability, which is possibly owing to the corrosion of Co in the acid media in the reaction. But combining with the results of continuous cyclic voltammetry tests in Fig. S12 that PtCo-3/NC still present excellent stability even for 15,000 cycles, it is supposed that the corrosion of Co does not have much impact on the prolonged durability of PtCo-3/NC to some extent. These results further illustrate the good prolonged durability on PtCo-3/NC. By the way, the atomic ratio of Pt:Co is not consistent well
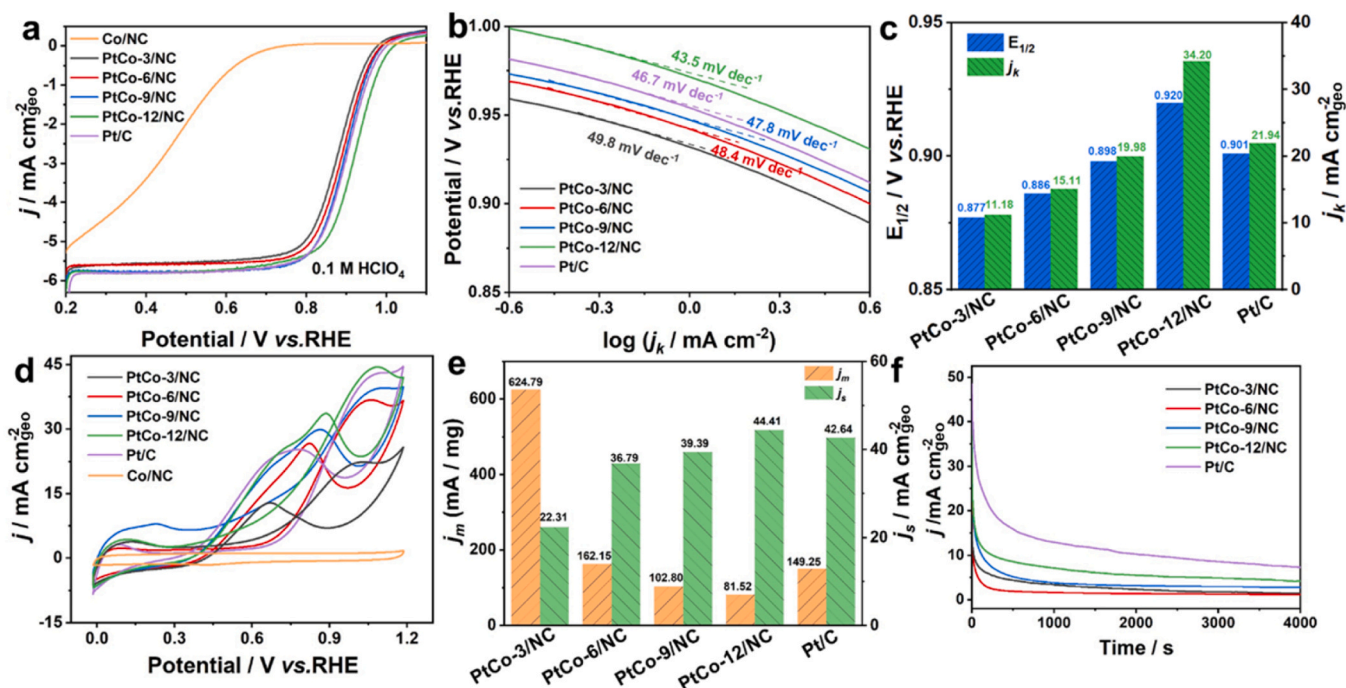
Fig. 3. Electrocatalytic behaviors of Co/NC, PtCo-3/NC, PtCo-6/NC, PtCo-9/NC, PtCo-12/NC and Pt/C in acidic media, respectively. (a) LSV curves in 0.1 M $HClO_4$; (b) The corresponding Tafel slope; (c) Statistical histograms of the upper half wave potential ($E_{1/2}$) of a series of PtCo/NC electrodes and Pt/C, and their kinetic current density (j_k) at 0.85 V; (d) Cyclic voltammograms (CVs) of each electrode in 1.0 M C_2H_5OH/0.1 M $HClO_4$ solution; (e) Histograms of the corresponding mass activities and specific activities; (f) Chronoamperograms of each electrode in 1.0 M C_2H_5OH/0.1 M $HClO_4$ solution.

with the results from ICP, probably due to the fact that EDS is a surface analysis technique which only take the local information from selected area.

As considering the promising applications in direct ethanol fuel cells (DEFCs), the PtCo/NC catalysts were also used as catalysts toward

ethanol electrooxidation [61–63]. The CVs in 1.0 M C_2H_5OH/0.1 M $HClO_4$ were recorded in Fig. 3d, and the peak current density were summarized in Fig. 3e. It can be seen that all PtCo/NC catalysts show excellent activity towards ethanol electrooxidation, and the peak potential was at around 1.05 V (vs. RHE). Note that specific area activity
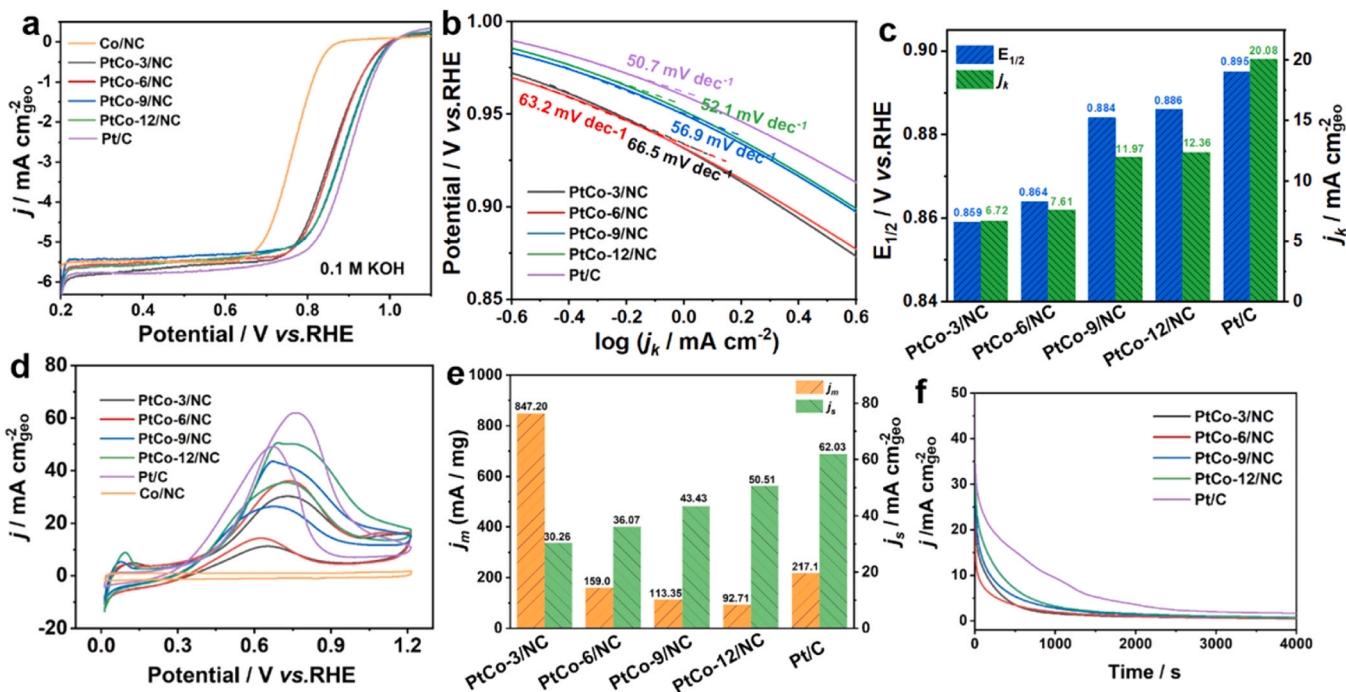

Fig. 4. Electrocatalytic behaviors of Co/NC, PtCo-3/NC, PtCo-6/NC, PtCo-9/NC, PtCo-12/NC and Pt/C in alkaline media, respectively. (a) LSV curves in 0.1 M KOH, respectively; (b) The corresponding Tafel slope; (c) Statistical histograms of the upper half wave potential ($E_{1/2}$) of each electrode and the kinetic current density (j_k) at 0.85 V; (d) Cyclic voltammograms (CVs) of each electrode in 1.0 M C_2H_5OH/1.0 M KOH solution; (e) Histograms of the corresponding mass activities and specific activities on those electrodes; (f) Chronoamperograms of each electrode in 1.0 M C_2H_5OH/1.0 M KOH solution.

on PtCo-3/NC, PtCo-6/NC, and PtCo-9/NC is lower than that on Pt/C (Fig. 3e), while the mass activity on them are superior to Pt/C, demonstrating the high utilization efficiency of Pt on PtCo/NC catalysts. In addition, when at the potential of 0.85 V (from ORR), the current density is 14.5, 19.0, 22.4, and 23.8 mA cm$_{geo}^{-2}$ towards ethanol electrooxidation, respectively, which is also summarized in (Table 1). These results suggest the promising high activity of the PtCo/NC catalysts at 0.85 V. The current density at 0.9 V are even higher than that at 0.85 V, summarized in Table S3. The poisoning tolerance of the PtCo/NC catalyst were further examined via the chronoamperometric i-t test at a constant potential of 0.85 V (vs. RHE), shown in Fig. 3f. It can be seen that all PtCo/NC catalysts also present good poisoning tolerance for the ethanol electrooxidation [61].

Besides of the acidic media, the ORR performances of PtCo/NC catalysts were also evaluated in O$_2$-saturated KOH. The LSVs on PtCo/NC catalysts and Pt/C are recorded in Fig. 4a, and the corresponding Tafel slope calculated via the Koutecky-Levich equation are shown in Fig. 4b, respectively. It can be seen in Fig. 4a that the activity on PtCo-9/NC and PtCo-12/NC are close to that on Pt/C in ORR in terms of the value of $E_{1/2}$ (0.88 V vs. 0.89 V, summarized in Fig. 4c), while PtCo-3/NC and PtCo-6/NC electrodes present a little lower activity than Pt/C, probably due to the much lower Pt loading on them, especially PtCo-3/NC. And from the Tafel slope summarized in Fig. 4b, the reaction dynamics on all PtCo/NC can be initially evaluated. In detail, the Tafel slope on those PtCo/NC catalysts are comparable to that on Pt/C (50.7 mV dec^{-1}), indicating high reaction dynamics in ORR on these PtCo/NC catalysts as Pt/C. Note that although PtCo-12/NC with higher Pt loading than Pt/C, the $E_{1/2}$ and Tafel slope on the former is lower than that on the latter. It is probably due to the fact that the calculated ECSA on PtCo-12/NC is smaller than that on Pt/C, resulting in a litter inferior catalytic activity as well as Tafel slope to the Pt/C (20 % Pt) in alkaline media in this work. The kinetic current density (j_k at 0.85 V) on all PtCo/NC catalysts are also summarized in Fig. 4c. Although these PtCo/NC catalysts show a little lower performances compared to Pt/C in alkaline media in this work, they still show comparable ORR activity to some similar materials in the literature in terms of the halfwave potential and limiting current density (summarized in Table S2), which further illustrate the promising enhancement of Co/NC substrate to ORR activity. The electron transfer number in alkaline media were determined on a catalyst-modified rotating disk electrode (RDE) as well, which are recorded in Figs. S15 and S16, respectively. Similar with the results in acid media, the average electron transfer number (n) for PtCo/NC catalysts is calculated as 3.7, comparable to that of the benchmark Pt/C (3.6, Fig. S16) in this work, indicating the 4e$^-$ oxygen reduction pathway on PtCo/NC-catalyst in alkaline media.

Similarly, the catalytic performances on those PtCo/NC catalysts toward ethanol electrooxidation were also investigated in 1.0 M C$_2$H$_5$OH/1.0 M KOH. The CVs were recorded in Fig. 4d, and the peak current density were summarized in Fig. 4e. It can be seen that the profile of the CVs in alkaline media is similar to that in acidic media. Although the specific area activity (j_s) on PtCo/NC catalysts is lower than that on Pt/C, the mass activity on them are much larger than that on Pt/C, also demonstrating the high utilization of Pt on PtCo/NC electrodes toward ethanol electrooxidation. In addition, at the limiting potential, e.g. 0.85 V (vs. RHE), all PtCo/NC catalysts show high current density toward ethanol electrooxidation in alkaline media, summarized in Table 1. The chronoamperometric i-t curves in Fig. 4f also demonstrate that the PtCo/NC catalysts present good poisoning tolerance for the ethanol electrooxidation. The above results suggest the potential with high reaction efficiency of PtCo/NC catalysts for both ORR and EOR in alkaline media.

As to look insight into the mechanism of the great catalytic activity on PtCo/NC, we supposed that besides of the morphology and geometry structure advantages on the as-fabricated catalysts as mentioned previously, there probably are strong metal-support interactions (MSI) between Pt and Co/NC substrate, which modulate the electronic structure

in the interface and promote the catalytic performance more effectively. Therefore, theoretical calculations based on DFT theory were implemented to explore the electronic state of elements, the charge transfer as well as the change of free energy [64]. For the modeling of the catalytic systems we used 6 × 6 supercell of four layers of graphene covered by two layers of hcp cobalt with 3 × 3 supercell and two layers of 3 × 3 supercell corresponding with (111) surface of fcc platinum (see Fig. 5a). For the sake of comprehensiveness, we also inserted nitrogen atom in pyridine position in each layer (Fig. 5a-c). To explore the effect of platinum layer, we performed calculations for described supercell with and without platinum cover. Since doublet lattice parameter of graphene almost coincides with lattice parameter of hcp lattice of cobalt, formation of Co/C and Co/N-C interface does not provide visible changes neither in carbon substrate nor in Co cover. On the contrary, mismatch between lattice parameters of fcc lattice of Pt and hcp lattice of Co leads to visible distortion of platinum cover.

Results of the calculations demonstrate that the steps of ORR over uncovered cobalt substrate corresponding with large negative energies (see Fig. 5d). By the other words, uncovered cobalt substrate should be irreversible hydrogenated or oxidized at the first steps of considered reactions. By contrast, formation of rather thin (two layers) platinum cover provides significant changes of chemical properties of the system. As seen, in the case of ORR, the magnitude of the free energies for PtCo/C substrate (−0.91 eV) is slightly larger than that for platinum (−0.89 eV), and nitrogen doping in carbon substrate makes PtCo/NC composite superior over platinum catalyst (−0.77 eV vs. −0.89 eV). Thus based on results of the calculations, it can be proposed that disorder induced in platinum cover by Co/C substrate does not change catalytic properties of platinum layers a lot. On the contrary, doping of carbon substrate by nitrogen provides minor but valuable improvement of the catalytic performance of platinum layer. Based on these results, we can propose that formation of PtCo/NC interfaces is good approach to decrease of platinum content without shrinking catalytic performance.

To reveal the nature of the improvement of catalytic performance of Pt surface, we check electronic structure of the system that shown in Fig. 5a. Generally, high catalytic performance associated with the peaks in vicinity of Fermi level. Despite the absence of these features in total density of states, which characterize whole system, electronic structure of 5d orbitals of surface platinum atoms have these peaks (labelled with stars in Fig. 5e). Note that these two peaks in electronic structure of Pt 5d almost coincide with similar features in electronic structure 2p orbitals of nitrogen atom from the layer closest to the interface with Co (these peaks are marked in Fig. 5e). More importantly, formation of the interface also leads to the shift of the center Pt 5d band from − 2.25 to − 2.12 eV. This shift is corresponding with enhancement of catalytic activity. Thus we can propose that due to the MSI between Pt and Co/NC substrate, peculiarities in electronic structure of CN influence electronic structure at the surface of Pt-layer. To prove this hypothesis, we calculate the changes of the differential charge densities after formation of the interfaces between N doped C, Co and Pt. Results of the calculations (see Fig. 5f) demonstrate the increasing charge density even in the layers of platinum, which is remote from the interface with cobalt. The differential charge densities diagram shown in Fig. 5f also reveals the role of Co-layers in the systems: the largest changes of the charge density are corresponding with these cobalt layers and nearest layers of CN and Pt. Thus we can propose that Co-layers amplify (or enhance) the effect of CN substrate on Pt surface.

To further test the potential application of the prepared PtCo/NC catalysts, homemade zinc-air batteries (ZABs) were assembled by using the carbon paper-loaded PtCo/NC as air-cathode [65]. The maximum power density is 109.8 mW cm^{-2} at a current density of 180 mA cm^{-2} on PtCo-3/NC (Fig. 6a), which is higher than that of Pt/C (97.6 mW cm^{-2} at 160 mA cm^{-2}); and the power density on the other as-prepared PtCo/NC catalysts is also close even superior to that of Pt/C, summarized in Table S4. The maximum power density on these PtCo/NC
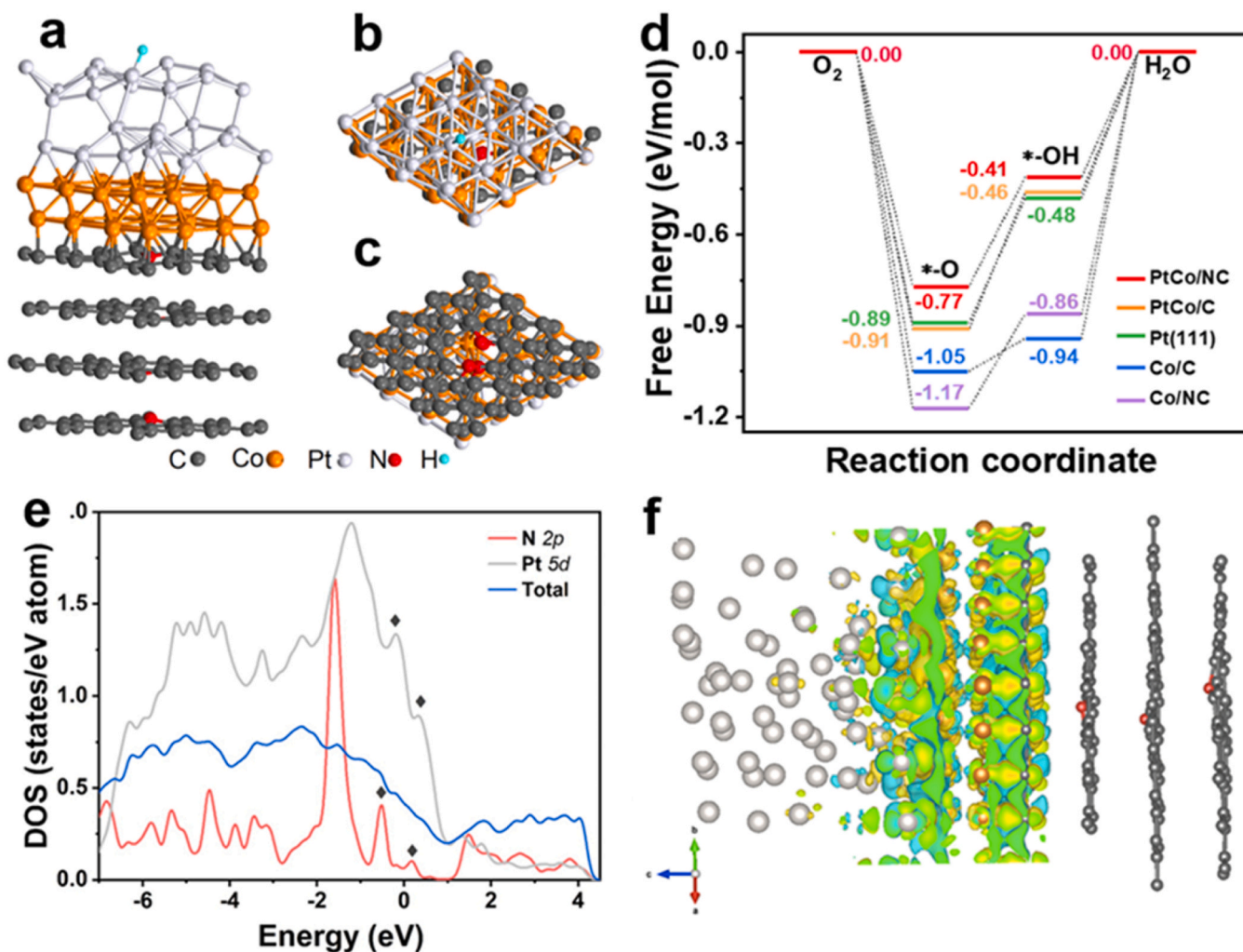
Fig. 5. Optimized atomic structures PtCo/NC slabs: (a) Side; (b) Top and (c) Bottom view, respectively; (d) The calculated free energy diagrams for ORR; (e) The density of states (DOS) of PtCo/NC and partial density of states of N and Pt in PtCo/NC; and (f) Differential charge densities diagram of PtCo/NC.

catalysts in this work were also compared with some similar materials in the literature, which is summarized in Table S2. As seen, some non-Pt and/or nonnoble metal based catalyst show superior power density to PtCo/NC catalysts in the as-assembled ZABs, although they show inferior $E_{1/2}$ to PtCo/NC catalysts. According to Qiao's work [66], this can be ascribed to the fact that, excepting the testing parameters (such as electrode distance, electrolyte concentration, and oxygen flux) and the preparation of catalysts ink (such as carbon materials and the amounts of PTFE) that would affect the power density of ZABs during assembling and testing process, another important factor is the surface structure of catalysts. It has been proved that a combination of nano and micro structures is highly favorable to accelerate gas diffusion. For example, in their study, Ni-doped CoO catalysts exhibit micro sized nanosheets with inside numerous nanosized pores, with this morphological advantage, the non-noble materials based ZABs could thereby present exceeded power density compared with the undefeatable Pt/C catalysts based device. The galvanostatic discharge capacities of PtCo/NC and Pt/C based ZABs were measured at 10 mA cm^{-2} at room temperature, recorded in Fig. 6b. The specific capacity of the as-assembled ZABs was normalized to the mass of consumed zinc. It can be seen that, the discharge voltages of both PtCo/NC and Pt/C based ZABs are all around 1.15 V. The calculated specific capacity of the PtCo-12/NC based ZAB is 1112 mAh g$_{Zn}^{-1}$, higher than that of Pt-based ZAB (972 mAh g$_{Zn}^{-1}$); and the specific capacity on the other PtCo/NC-based ZABs are close to 900 mAh g$_{Zn}^{-1}$. By the way, the drop in discharge curves represents the passivation

and the deposition of ZnO particles on the surface of Zn anode, which limits the utilization efficiency of Zn during discharging. The rate-discharge curves over various discharge current densities of the PtCo/NC catalyst-based ZAB are shown in Fig. 6c, in which a stable plateau can be observed at each discharge current density. In addition, two pairs of PtCo/NC catalyst-based ZAB connect in-series and successfully power a light-emitting diode (Fig. 6d), demonstrating that the as-obtained PtCo/NC catalyst is a promising ORR catalyst for actual power devices.

The hydrogen evolution performances were also explored via linear sweep voltammetry (LSV) in 0.5 M H$_2$SO$_4$ and 1.0 M KOH electrolyte, respectively, aiming to look insight into the effect of MSI on PtCo-X/NC for HER. As shown in Fig. S17a, all PtCo-X/NC catalysts show unexpected superior HER activity with quite low overpotential in acidic media (the insert in Fig. S17a), in detail, 21, 10, 16, and 18 mV on PtCo-3/NC, PtCo-6/NC, PtCo-9/NC, and PtCo-12/NC at the current density of 10 mA cm^{-2}, respectively, which are much lower than that on Pt/C (45 mV). At the current density of 50 mA cm^{-2}, the overpotentials on PtCo/NC samples are also close even superior to that of the commercial Pt/C (90 mV). The Tafel slope of PtCo/NC catalysts shown in Fig. S17b is very close to that of Pt/C, indicating high reaction kinetics on PtCo/NC catalysts with low HER energy barrier. Meanwhile, the measured low Tafel slope of all PtCo/NC catalysts suggests a Volmer-Tafel mechanism on them [62]. The performed lower overpotential and Tafel slope demonstrate that the PtCo/NC catalysts have excellent catalytic
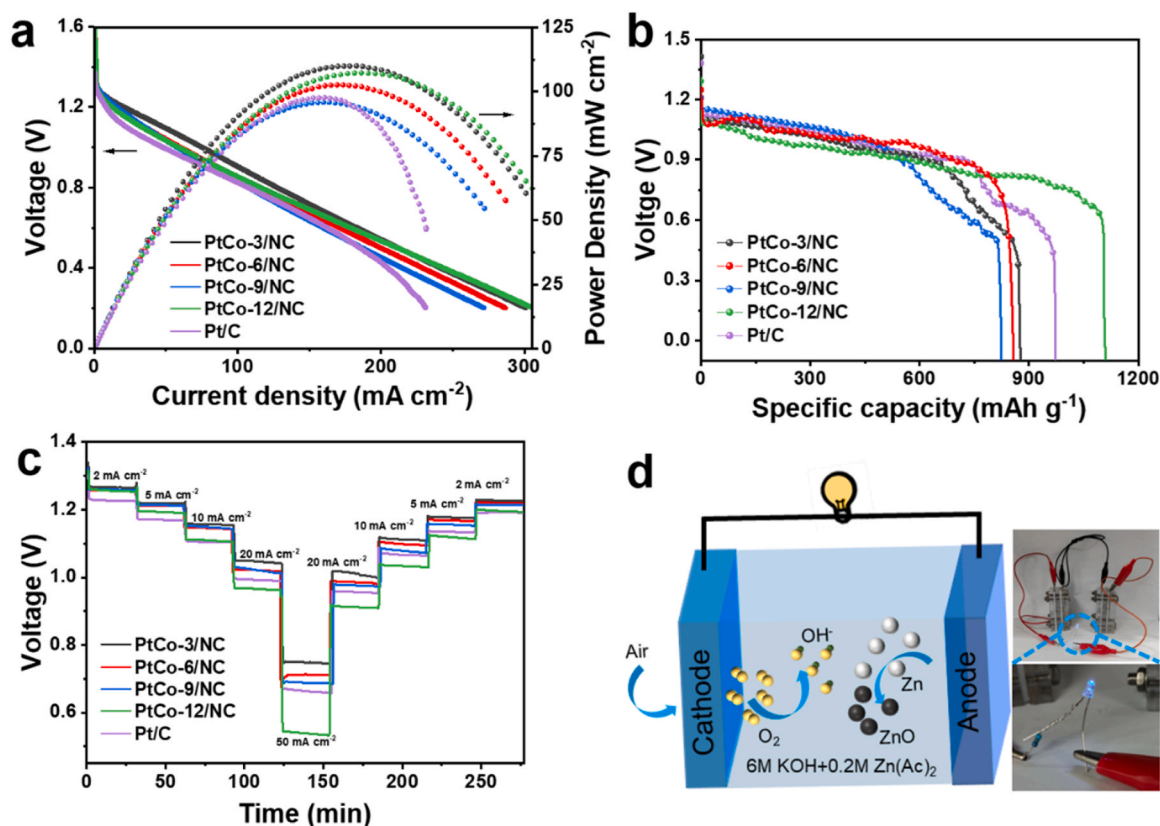
Fig. 6. The performances of PtCo-X/NC and Pt/C as the air cathode assembled in zinc-air battery, respectively. (a) Discharge polarization curves and the corresponding power density curves; (b) Discharge specific capacity profiles at the current density of 10 mA cm^{-2}; (c) Galvanostatic discharge profile at 2–50 mA cm^{-2} of PtCo/NC and Pt/C based ZABs, respectively; (d) Schematic illustration of the structure of Zn-air battery (insert: Image of blue LED energized by two PtCo/NC based Zn-air batteries in series).

performances toward HER [67,68], especially PtCo-3/NC with ultralow Pt loading. The stability and durability were characterized on PtCo-6/NC via continuous cyclic voltammetry test and chronoamperometry, shown in Fig. S17c. It can be seen that PtCo-6/NC presents remarkable long-term durability for HER in acid media. The performances of PtCo/NC toward HER were similarly tested in 1.0 M KOH solution. The curves are recorded in Fig. S18, and the corresponding values are summarized in Table S5. PtCo-X/NC catalysts present comparable overpotential and Tafel slope to Pt/C, demonstrating excellent HER activity on PtCo-X/NC catalysts in alkaline media. The calculations results (Fig. S19) show that, although the free energy of HER steps turns from negative to positive, the magnitude of the energies (~0.16 eV for PtCo/C and ~0.06 eV for PtCo/NC) is compatible with the magnitude of the free energy calculated for Pt(111) surface (~−0.1 eV). The excellent catalytic performances on PtCo/NC in HER in both acid and alkaline media are supposed to attributed to the strong MSI between Pt and Co/NC that, the change of electronic structure and the distribution of charge density effectively optimize catalytic behaviors of PtCo/NC.

4. Conclusions

In summary, tri-functional PtCo/NC bimetal nanocatalysts with ultralow Pt loading supported on ZIF-67 derived porous carbonaceous material were fabricated and used as electrocatalysts for ORR, EOR and HER in both acidic and alkaline media. Besides of strong adhesion between the hybrid Pt catalyst as well as the advantages of N-doped carbon support and the morphology structure, there probably are strong MSI between Pt and Co/NC which further promote the catalytic performances of PtCo/NC. The results of DFT based theoretical calculation

elaborated that, the electronic structure of N-doped C influences electronic structure of surface Pt-layer, leading to the redistribution of charge density, and Co-layers close to N further enhance this effect of CN substrate on Pt-surface; meanwhile, nitrogen doping of carbon substrate makes PtCo/NC composite superior over platinum catalyst in free energy, which means PtCo/NC is more energetically favorable than Pt/C. Notably, PtCo-3/NC that has ultralow Pt loading (1 %) exhibits $E_{1/2}$ of 0.877 V in acidic media, which is comparable to commercial Pt/C and many similar materials with higher Pt loading; with the increase of Pt loading, the $E_{1/2}$ on PtCo-9/NC (0.898 V) and PtCo-12/NC (0.920 V) is almost equal even superior to commercial Pt/C (0.901 V). In addition, the as-prepared PtCo/NC catalysts also present high current density toward ethanol oxidation reaction (EOR) at 0.85 V and outstanding low overpotential of 10 mV at 10 mA cm^{-2} for HER. Furthermore, the as-assembled ZABs based on PtCo/NC catalysts as air cathode presents higher specific power density than Pt/C-based ZAB as well. Our work provides a promising way to construct Pt catalysts with ultralow Pt-loading but comparable catalytic performances to Pt/C, and highlights its possibility as highly effectively electrode catalysts for the practical applications in direct ethanol fuel cells as well as metal-air battery.

CRediT authorship contribution statement

Zhang Manting: Conceptualization, Validation, Formal analysis, Investigation, Writing – original draft. **Zhou Tingting:** Resources, Data curation. **Bukhvalov Danil:** Software. **Han Fengyan:** Resources, Investigation, Validation. **Wang Caiqin:** Supervision, Conceptualization, Writing – review & editing, Project administration, Funding acquisition. **Yang Xiaofei:** Project administration, Funding acquisition.

Declaration of Competing Interest

The authors declare that they have no known competing financial interests or personal relationships that could have appeared to influence the work reported in this paper.

Data availability

Data will be made available on request.

Appendix A. Supporting information

Supplementary data associated with this article can be found in the online version at doi:10.1016/j.apcatb.2023.122976.

References

[1] X. Li, Y. Yan, X. Zheng, Y. Yao, Y. Liu, Atomically dispersed V-N-C catalyst with saturated coordination effect for boosting electrochemical oxygen reduction, Chem. Eng. J. 444 (2022), 136363.

[2] W. Tian, J. Ren, Z. Yuan, In-situ cobalt-nickel alloy catalyzed nitrogen-doped carbon nanotube arrays as superior freestanding air electrodes for flexible zinc-air and aluminum-air batteries, Appl. Catal. B 317 (2022), 121764.

[3] X. Sun, Y. Li, H. Su, X. Zhang, Y. Xu, W. Zhou, M. Liu, W. Cheng, Q. Liu, Dissecting π-conjugated covalent-coupling over conductive mofs toward efficient two-electron oxygen reduction, Appl. Catal. B 317 (2022), 121706.

[4] M. Gopalakrishnan, A. Mohamad, M. Nguyen, T. Yonezawa, J. Qin, P. Thamyongkit, A. Somwangthanaroj, S. Kheawhom, Recent advances in oxygen electrocatalysts based on tunable structural polymers, Mater. Today Chem. 23 (2022), 100632.

[5] S. Bhoyate, J. Kim, F. Souza, J. Lin, E. Lee, A. Kumar, R. Gupta, Science and engineering for non-noble-metal-based electrocatalysts to boost their ORR performance: a critical review, Coord. Chem. Rev. 474 (2023), 214854.

[6] B. Xu, Y. Zhang, L. Li, Q. Shao, X. Huang, Recent progress in low-dimensional palladium-based nanostructures for electrocatalysis and beyond, Coord. Chem. Rev. 459 (2022), 214388.

[7] S. Zhao, C. Tan, C. He, P. An, F. Xie, S. Jiang, Y. Zhu, K. Wu, B. Zhang, H. Li, J. Zhang, Y. Chen, S. Liu, J. Dong, Z. Tang, Structural transformation of highly active metal-organic framework electrocatalysts during the oxygen evolution reaction, Nat. Energy 5 (2020) 881–890.

[8] H. Wang, L. Chen, H. Pang, S. Kaskel, Q. Xu, MOF-derived electrocatalysts for oxygen reduction, oxygen evolution and hydrogen evolution reactions, Chem. Soc. Rev. 49 (2020) 1414–1448.

[9] Z. Chen, X. Duan, W. Wei, S. Wang, B. Ni, Iridium-based nanomaterials for electrochemical water splitting, Nano Energy 78 (2020), 105270.

[10] S. Zhao, T. Liu, Y. Dai, J. Wang, Y. Wang, Z. Guo, J. Yu, I. Bello, M. Ni, Pt/C as a bifunctional ORR/iodide oxidation reaction (IOR) catalyst for Zn-air batteries with unprecedentedly high energy efficiency of 76.5%, Appl. Catal. B 320 (2023), 121992.

[11] J. Hansen, H. Prats, K. Toudahl, N. Morch Secher, K. Chan, J. Kibsgaard, I. Chorkendorff, Is there anything better than Pt for HER, ACS Energy Lett. 6 (2021) 1175–1180.

[12] X. Li, Y. He, S. Cheng, B. Li, Y. Zeng, Z. Xie, Q. Meng, L. Ma, K. Kisslinger, X. Tong, S. Hwang, S. Yao, C. Li, Z. Qiao, C. Shan, Y. Zhu, J. Xie, G. Wang, G. Wu, D. Su, Atomic structure evolution of Pt-Co binary catalysts: single metal sites versus intermetallic nanocrystals, Adv. Mater. 33 (2021) 2106371.

[13] Y. Luo, Y. Wang, Y. Wang, H. Huang, L. Zhang, H. Zhang, Y. Wang, Illumination enabling monoatomic Fe and Pt-based catalysts on NC/TiO for efficient and stable oxygen reduction, Appl. Catal. B 317 (2022), 121797.

[14] Y. Kim, H. Bae, D. Lee, J. Kim, E. Lee, S. Oh, J. Jang, Y. Cho, M. Karuppannan, Y. Sung, T. Lim, O. Kwon, High-performance long-term driving proton exchange membrane fuel cell implemented with chemically ordered Pt-based alloy catalyst at ultra-low pt loading, J. Power Sources 533 (2022), 231378.

[15] J. Zhang, Y. Yuan, L. Gao, G. Zeng, M. Li, H. Huang, Stabilizing Pt-based electrocatalysts for oxygen reduction reaction: fundamental understanding and design strategies, Adv. Mater. 33 (2021), 2006494.

[16] M. Wei, L. Huang, L. Li, F. Ai, J. Su, J. Wang, Coordinatively unsaturated PtCo flowers assembled with ultrathin nanosheets for enhanced oxygen reduction, ACS Catal. 12 (2022) 6478–6485.

[17] K. Kodama, T. Nagai, A. Kuwaki, R. Jinnouchi, Y. Morimoto, Challenges in applying highly active Pt-based nanostructured catalysts for oxygen reduction reactions to fuel cell vehicles, Nat. Nanotechnol. 16 (2021) 140–147.

[18] Y. Yang, Y. Yang, Y. Liu, S. Zhao, Z. Tang, Metal-organic frameworks for electrocatalysis: beyond their derivatives, Small, Sci 1 (2021), 2100015.

[19] R. Mo, X. Zhang, Z. Chen, S. Huang, Y. Li, L. Liang, Z. Tian, P. Shen, Highly efficient PtCo nanoparticles on Co-N-Cnanorods with hierarchical pore structure for oxygen reduction reaction, Int. J. Hydrog. Energy 46 (2021) 15991–16002.

[20] L. Liang, H. Jin, H. Zhou, B. Liu, C. Hu, D. Chen, Z. Wang, Z. Hu, Y. Zhao, H. Li, D. He, S. Mu, Cobalt single atom site isolated Pt nanoparticles for efficient ORR and HER in acid media, Nano Energy 88 (2021), 106221.

[21] X. Han, Q. Wang, Z. Zheng, Z. Nan, X. Zhang, Z. Song, M. Ma, J. Zheng, Q. Kuang, L. Zheng, Size-controlled intermetallic PtZn nanoparticles on N-doped carbon support for enhanced electrocatalytic oxygen reduction, ACS Sustain. Chem. Eng. J. 9 (2021) 3821–3827.

[22] Y. Xue, H. Li, X. Ye, S. Yang, Z. Zheng, X. Han, X. Zhang, L. Chen, Z. Xie, Q. Kuang, L. Zheng, N-doped carbon shell encapsulated PtZn intermetallic nanoparticles as highly efficient catalysts for fuel cells, Nano Res. 12 (2019) 2490–2497.

[23] S. Zhao, Y. Yang, Z. Tang, Insight into structural evolution, active sites, and stability of heterogeneous electrocatalysts, Angew. Chem. Int. Ed. 61 (2022), e202110186.

[24] X. Zhao, X. Yang, M. Wang, S. Hwang, S. Karakalos, M. Chen, Z. Qiao, L. Wang, B. Liu, Q. Ma, D. Cullen, D. Su, H. Yang, H. Zang, Z. Feng, G. Wu, Single-iron site catalysts with self-assembled dual-size architecture and hierarchical porosity for proton-exchange membrane fuel cells, Appl. Catal. B 279 (2020), 119400.

[25] C. Yang, X. Ma, J. Zhou, Y. Zhao, X. Xiang, H. Shang, B. Zhang, Recent advances in metal-organic frameworks-derived carbon-based electrocatalysts for the oxygen reduction reaction, Int. J. Hydrog. Energy 47 (2022) 21634–21661.

[26] S. Zhao, Y. Wang, J. Dong, C. He, H. Yin, P. An, K. Zhao, X. Zhang, C. Gao, L. Zhang, J. Lv, J. Wang, J. Zhang, A. Khattak, N. Khan, Z. Wei, J. Zhang, S. Liu, H. Zhao, Z. Tang, Ultrathin metal-organic framework nanosheets for electrocatalytic oxygen evolution, Nat. Energy 1 (2016) 16184.

[27] C. Gao, S. Mu, R. Yan, F. Chen, T. Ma, S. Cao, S. Li, L. Ma, Y. Wang, C. Cheng, Recent advances in ZIF-derived atomic metal-N-C electrocatalysts for oxygen reduction reaction: synthetic strategies, active centers, and stabilities, Small 18 (2022), 2105409.

[28] K. Yuan, D. Lutzenkirchen-Hecht, L. Li, L. Shuai, Y. Li, R. Cao, M. Qiu, X. Zhuang, M. Leung, Y. Chen, U. Scherf, Boosting oxygen reduction of single iron active sites via geometric and electronic engineering: nitrogen and phosphorus dual coordination, J. Am. Chem. Soc. 142 (2020) 2404–2412.

[29] L. Yang, X. Zeng, W. Wang, D. Cao, Recent progress in MOF-derived, heteroatom-doped porous carbons as highly efficient electrocatalysts for oxygen reduction reaction in fuel cells, Adv. Funct. Mater. 28 (2018) 1704537.

[30] L. Zhao, C. Fu, L. Luo, J. You, L. An, X. Yan, S. Shen, J. Zhang, Electrochemical synthesis of monodispersed and highly alloyed PtCo nanoparticles with a remarkable durability towards oxygen reduction reaction, Appl. Catal. B 318 (2022), 121831.

[31] F. Guo, Z. Zou, Z. Zhang, T. Zeng, Y. Tan, R. Chen, W. Wu, N. Cheng, X. Sun, Confined sub-nanometer PtCo clusters as a highly efficient and robust electrocatalyst for the hydrogen evolution reaction, J. Mater. Chem. A 9 (2021) 5468–5474.

[32] Y. Sun, B. Huang, Y. Li, Y. Xing, M. Luo, N. Li, Z. Xia, Y. Qin, D. Su, L. Wang, S. Guo, Trifunctional fishbone-like PtCo/Ir enables high-performance zinc-air batteries to drive the water-splitting catalysis, Chem. Mater. 31 (2019) 8136–8144.

[33] G. Zhi, W. Wang, Y. Zhou, L. Feng, ZIF-67-derived CoP/NC effectively supported Pt nanoparticles for methanol oxidation reaction, Nanoscale 15 (2023) 2948–2953.

[34] S. Li, J. Liu, J. Liang, Z. Lin, X. Liu, Y. Chen, G. Lu, C. Wang, P. Wei, J. Han, Y. Huang, G. Wu, Q. Li, Tuning oxygen vacancy in SnO₂ inhibits Pt migration and agglomeration towards high-performing fuel cells, Appl. Catal. B 320 (2023), 122017.

[35] S. Feng, J. Chen, G. Qian, Y. Mo, J. Lu, W. Chen, L. Luo, S. Yin, Metal-support interactions in a molybdenum oxide anchored PtNi alloy for improving oxygen reduction activity, ACS Appl. Energy Mater. 3 (2020) 12246–12253.

[36] J. Li, S. Zou, X. Liu, Y. Lu, D. Dong, Electronically modulated CoP by Ce doping as a highly efficient electrocatalyst for water splitting, ACS Sustain. Chem. Eng. 8 (2020) 10009–10016.

[37] P. Giannozzi, S. Baroni, N. Bonini, M. Calandra, R. Car, C. Cavazzoni, QUANTUM ESPRESSO: a modular and open-source software project for quantum simulations of materials, J. Phys. 21 (2009), 395502.

[38] J. Perdew, K. Burke, M. Ernzerhof, Generalized gradient approximation made simple, Phys. Rev. Lett. 77 (1996) 3865–3868.

[39] V. Barone, M. Casarin, D. Forrer, M. Pavone, M. Sambi, A. Vittadini, Role and effective treatment of dispersive forces in materials: polyethylene and graphite crystals as test cases, J. Comput. Chem. 30 (2009) 934–939.

[40] D. Vanderbilt, Soft self-consistent pseudopotentials in a generalized eigenvalue formalism, Phys. Rev. B 41 (1990) 7892–7895.

[41] J. Greeley, T. Jaramillo, J. Bonde, I. Chorkendorff, J. Nørskov, Computational high-throughput screening of electrocatalytic materials for hydrogen evolution, Nat. Mater. 5 (2006) 909–913.

[42] Y. Tang, B. Allen, D. Kauffman, A. Star, Electrocatalytic activity of nitrogen-doped carbon nanotube cups, J. Am. Chem. Soc. 131 (2009) 13200–13201.

[43] H. Hansen, J. Rossmeisl, J. Nørskov, Surface pourbaix diagrams and oxygen reduction activity of Pt, Ag and Ni(111) surfaces studied by DFT, Phys. Chem. Chem. Phys. 10 (2008) 3722–3730.

[44] J. Nørskov, J. Rossmeisl, A. Logadottir, L. Lindqvist, J. Kitchin, T. Bligaard, H. Jonsson, Origin of the overpotential for oxygen reduction at a fuel-cell cathode, J. Phys. Chem. B 108 (2004) 17886–17892.

[45] S. Ramakrishnan, M. Karuppannan, M. Vinothkannan, K. Ramachandran, O. Kwon, D. Yoo, Ultrafine Pt nanoparticles stabilized by MoS$_2$/N-doped reduced graphene oxide as a durable electrocatalyst for alcohol oxidation and oxygen reduction reactions, ACS Appl. Mater. Interfaces 11 (2019) 12504–12515.

[46] X. Song, Y. He, B. Wang, S. Peng, L. Tong, Q. Liu, J. Yu, H. Tang, PtNi alloy coated in porous nitrogen-doped carbon as highly efficient catalysts for hydrogen evolution reactions, Molecules 27 (2022) 499.

[47] J. Lu, Y. Li, S. Li, S. Jiang, Self-assembled platinum nanoparticles on sulfonic acid-grafted graphene as effective electrocatalysts for methanol oxidation in direct methanol fuel cells, Sci. Rep. 6 (2016) 21530.

[48] C. Cheng, J. Lin, K. Huang, T. Yeh, C. Hsieh, Enhanced efficiency of dye-sensitized solar counter electrodes consisting of two-dimensional nanostructural molybdenum disulfide nanosheets supported Pt nanoparticles, Coatings 7 (2017) 167.

[49] Y. Yin, X. Liu, X. Wei, Y. Li, X. Nie, R. Yu, J. Shui, Magnetically aligned Co-C/MWCNTs composite derived from MWCNT-interconnected zeolitic imidazolate frameworks for a lightweight and highly efficient electromagnetic wave absorber, ACS Appl. Mater. Interfaces 9 (2017) 30850–30861.

[50] Y. Chen, S. Jie, C. Yang, Z. Liu, Active and efficient Co-N/C catalysts derived from cobalt porphyrin for selective oxidation of alkylaromatics, Appl. Surf. Sci. 419 (2017) 98–106.

[51] Q. Liu, X. Liu, H. Feng, H. Shui, R. Yu, Metal organic framework-derived Fe/carbon porous composite with low Fe content for lightweight and highly efficient electromagnetic wave absorber, Chem. Eng. J. 314 (2017) 320–327.

[52] Y. Zhang, Y. You, S. Xin, Y. Yin, J. Zhang, P. Wang, X. Zheng, F. Cao, Y. Guo, Rice husk-derived hierarchical silicon/nitrogen-doped carbon/carbon nanotube spheres as low-cost and high-capacity anodes for lithium-ion batteries, Nano Energy 25 (2016) 120–127.

[53] Y. Pan, K. Sun, S. Liu, X. Cao, K. Wu, W. Cheong, Z. Chen, Y. Wang, Y. Li, Y. Liu, D. Wang, Q. Peng, C. Chen, Y. Li, Core-shell ZIF-8@ZIF-67-derived CoP nanoparticle-embedded N-doped carbon nanotube hollow polyhedron for efficient overall water splitting, J. Am. Chem. Soc. 140 (2018) 2610–2618.

[54] W. Wang, H. Wang, Y. Yu, Z. Wu, M. Asif, H. Liu, Metallic cobalt modified MnO-C nanocrystalline composites as an efficient bifunctional oxygen electrocatalyst, Catal. Sci. Technol. 8 (2018) 480–485.

[55] M. Sun, S. Yun, J. Dang, Y. Zhang, Z. Liu, D. Qiao, 1D/3D rambutan-like mott-schottky porous carbon polyhedrons for efficient tri-iodide reduction and hydrogen evolution reaction, Chem. Eng. J. 458 (2023), 141301.

[56] J. Adams, M. Kromer, J. Rodriguez-Lopez, D. Flaherty, Unifying concepts in electro- and thermocatalysis toward hydrogen peroxide production, J. Am. Chem. Soc. 143 (2021) 7940–7957.

[57] Y. Liu, Y. Shen, S. Zhu, D. Li, Tin nanoparticles hybridized with Fe, N co-doped carbon nanosheets composites as highly efficient electrocatalyst for oxygen reduction reaction, Chem. Eng. J. 400 (2020), 125968.

[58] L. Song, T. Zheng, L. Zheng, B. Lu, H. Chen, Q. He, W. Zheng, Y. Hou, J. Lian, Y. Wu, J. Chen, Z. Ye, J. Lu, Cobalt-doped basic iron phosphate as bifunctional electrocatalyst for long-life and high-power-density rechargeable zinc-air batteries, Appl. Catal. B 300 (2022), 120712.

[59] M. Fan, Q. Yuan, Y. Zhao, Z. Wang, A. Wang, Y. Liu, K. Sun, J. Wu, L. Wang, J. Jiang, A facile "double-catalysts" approach to directionally fabricate pyridinic Nb-pair-doped crystal graphene nanoribbons/amorphous carbon hybrid electrocatalysts for efficient oxygen reduction reaction, Adv. Mater. 34 (2022) 2107040.

[60] L. Zhang, J. Fischer, Y. Jia, X. Yan, W. Xu, X. Wang, J. Chen, D. Yang, H. Liu, L. Zhuang, M. Hankel, D. Searles, K. Huang, S. Feng, C. Brown, X. Yao, Coordination of atomic Co-Pt coupling species at carbon defects as active sites for oxygen reduction reaction, J. Am. Chem. Soc. 140 (2018) 10757–10763.

[61] J. Gao, X. Zhou, Y. Wang, Y. Chen, Z. Xu, Y. Qiu, Q. Yuan, X. Lin, H. Qiu, Exploiting the synergistic electronic interaction between Pt-skin wrapped intermetallic PtCo nanoparticles and Co-N-C support for efficient ORR/EOR electrocatalysis in a direct ethanol fuel cell, Small 18 (2022), 2202071.

[62] A. Rodríguez-Gómez, F. Dorado, P. Sánchez, A. de la Osa, Boosting hydrogen and chemicals production through ethanol electro-reforming on Pt-transition metal anodes, J. Energy Chem. 70 (2022) 394–406.

[63] J. Wang, J. Zhang, G. Liu, C. Ling, B. Chen, J. Huang, X. Liu, B. Li, A. Wang, Z. Hu, M. Zhou, Y. Chen, H. Cheng, J. Liu, Z. Fan, N. Yang, C. Tan, L. Gu, J. Wang, H. Zhang, Crystal phase-controlled growth of PtCu and PtCo alloys on 4h Au nanoribbons for electrocatalytic ethanol oxidation reaction, Nano Res. 13 (2020) 1970–1975.

[64] T. Liu, Y. Jing, Y. Li, Two-dimensional biphenylene: a graphene allotrope with superior activity toward electrochemical oxygen reduction reaction, J. Phys. Chem. Lett. 12 (2021) 12230–12234.

[65] N. Logeshwaran, S. Ramakrishnan, S. Chandrasekaran, M. Vinothkannan, A. Kim, S. Sengodan, P. Velusamy, P. Varadhan, J. He, D. Yoo, An efficient and durable trifunctional electrocatalyst for zinc-air batteries driven overall water splitting, Appl. Catal. B 297 (2021), 120405.

[66] D. Jiao, Z. Ma, J. Li, Y. Han, J. Mao, T. Ling, S. Qiao, Test factors affecting the performance of zinc-air battery, J. Energy Chem. 44 (2020) 1–7.

[67] S. Wang, Y. Cao, W. Jia, Z. Lu, D. Jia, A cage-confinement strategy to fabricate Pt-Mo$_6$Co$_6$C heterojunction for highly efficient pH-universal hydrogen evolution, Appl. Catal. B 298 (2021), 120579.

[68] Z. Wu, P. Yang, Q. Li, W. Xiao, Z. Li, G. Xu, F. Liu, B. Jia, T. Ma, S. Feng, L. Wang, Microwave synthesis of Pt clusters on black TiO$_2$ with abundant oxygen vacancies for efficient acidic electrocatalytic hydrogen evolution, Angew. Chem. Int. Ed. 62 (2023), e202300406.